Materials Characterization 225 (2025) 115139

Contents lists available at ScienceDirect

Materials Characterization

journal homepage: www.elsevier.com/locate/matchar

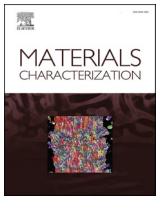

Microstructure characterization of AlCrFeCoNi high-entropy alloy coating on Inconel 718 by electrospark deposition

Jihui Yan [a], Joao G. Lopes [b], Kevin Chan [c], Nigel Scotchmer [c], Joao P. Oliveira [d], Y. Norman Zhou [a], Peng Peng [a,*]

[a] Centre for Advanced Materials Joining (CAMJ), Department of Mechanical and Mechatronics Engineering, University of Waterloo, 200 University Ave W, Waterloo, Ontario N2L 3G1, Canada
[b] UNIDEMI, Department of Mechanical and Industrial Engineering, NOVA School of Science and Technology, Universdade NOVA de Lisboa, Caparica 2829-516, Portugal
[c] Huys Industries Ltd., 7 Vulcan St, Etobicoke, Ontario M9W 1L3, Canada
[d] CENIMAT/I3N, Department of Materials Science, NOVA School of Science and Technology, Universdade NOVA de Lisboa, Caparica 2829-516, Portugal

ARTICLE INFO

Keywords:
Electrospark deposition
High entropy alloy
Coating
Microstructure
Heat treatment
Nano-indentation
Wear test

ABSTRACT

Recent scientific advancements in the field of high entropy alloys have sparked significant interest due to their exceptional performance across diverse environments. These properties are particularly valuable in surface protection engineering, where the selection of appropriate coating materials can profoundly impact the cost and properties of high-performance components. Consequently, understanding their compatibility with conventional engineering alloys is crucial. This study presents a detailed microstructural analysis of as-deposited and heat-treated AlCrFeCoNi HEA coatings on Inconel 718 substrate, fabricated via electrospark deposition. The as-deposited coatings exhibited cellular grains predominantly composed of the BCC phase, showing minimal elemental segregation. Subsequent heat treatment induced FCC and σ precipitate formation in the coatings, leading to noticeable elemental and phase segregation. Comprehensive characterization using X-ray diffraction, nano-indentation, and microhardness testing investigate the metallurgical and mechanical properties of the fabricated coatings. Wear resistance tests demonstrated that HEA-based coatings hold promise for enhancing surface wear resistance.

1. Introduction

High entropy alloys (HEAs) have garnered increasing attention since their inception in 2004 [1] due to their exceptional mechanical properties, such as fracture toughness [2], and tensile strength [3,4]. These characteristics make HEAs highly competitive as structural workpieces [5,6] or functional components, such as coating and catalysts [7], when compared to conventional engineering alloys. With special regard to HEA coatings, they can provide significant surface protection for substrate, offering resistance to corrosion, thermal degradation, erosion, and wear.

Among the various available HEAs, the AlCrFeCoNi HEA stands out due to its multi-phase microstructure and superior properties, including high hardness and excellent compressive properties [8,9]. This HEA system has demonstrated good corrosion resistance [10] and wear performance [11], making it a promising candidate for coating application in corrosive and wear-intensive environments. Several coating techniques, such as laser cladding, thermal spray, and cold spray, have been employed to fabricate HEA-based coating. For instances, Chen et al. [12] fabricated a CrFeCoNiCu/AlCrFeCoNi HEA composite coating using laser cladding, which exhibited a remarkable balance between toughness and strength. On a different approach, Noble et al. [13] investigated the application of AlCrFeCoNi HEA coating on 316L steel using thermal spray, finding that it significantly enhanced wear resistance compared to the bare substrate. Anupam et al. [14] used cold spray to fabricated AlCrFeCoNi HEA coating on Ni-based superalloy, which showed high oxidation resistance due to the formation of aluminum oxide and molybdenum diffusion at temperature above 1000 °C.

However, these processes are associated with the need for high-quality powder feedstock and intricate process parameter optimization. Additionally, they require well-prepared surfaces to ensure proper coating adhesion and metallurgical bonding, involving high equipment

* Corresponding author.
E-mail address: peng.peng@uwaterloo.ca (P. Peng).

https://doi.org/10.1016/j.matchar.2025.115139
Received 21 October 2024; Received in revised form 23 April 2025; Accepted 6 May 2025
Available online 11 May 2025
1044-5803/© 2025 Elsevier Inc. All rights are reserved, including those for text and data mining, AI training, and similar technologies.

and operational costs. In contrast, electrospark deposition (ESD), a low-energy welding technique, presents several advantages. ESD has low requirements for feedstock and substrate quality, incurs low operational costs, and allows for straightforward process optimization, making it a competitive option for coating deposition [15].

In this work, an equiatomic AlCrFeCoNi HEA electrode was utilized as the feedstock to fabricate HEA coating on Inconel 718 using ESD. Post heat treatment was conducted to examine the microstructure and evaluate the properties of the coatings. Both the as-deposited and heat-treated coatings were analyzed in terms of microstructure and phase formation. The comprehensive characterizations, microhardness, nano-indentation, and wear test, provide a systematic evaluation of the mechanical performance of the coating.

2. Materials and methods

Inconel 718 plates with a thickness of 1.5 mm were utilized as substrate for the coating deposition process, which was performed using an ESD machine from Huys Industries under a 99.999% argon protective atmosphere. For such, rod-shaped electrodes, with a diameter of 3 mm, were machined via wire-EDM from commercially available equiatomic AlCrFeCoNi HEA ingot (acquired from Heeger Materials Inc).

The HEA rod was positioned in the applicator, and deposition was performed by contacting the substrate. The trial parameters are detailed in Table 1. Following coating deposition, a total of 4 samples were subjected to heat treatment performed under a 99.999% argon flow at 1050 °C for 4 h, and then rapidly cooled by submerging them in room temperature water. The selection of 1050 °C heat treatment is due to the phase transformation temperature from single phase to multiple phase based on AlCrFeCoNi phase diagram [16,17].

For microstructural characterization, the as-deposited (AD) and heat-treated (HT) coatings were mounted with conductive epoxy resin, ground up to 600 grid, and polished with 3 and 0.25 μm diamond polishing suspension. The samples were etched with Kalling's 2 reagent. Optical microscope (OM, Olympus BX51M), field emission scanning electron microscope (FE-SEM, Zeiss Leo 1530) equipped with energy dispersive X-ray (EDX, AMETEK EDAX Apollo XL) were used for microstructure observation. Additionally, electron backscattered diffraction (EBSD, JEOL 7000F SEM) and micro-XRD patterns (D8 Discover) with copper targeted at 1.5406 Å were used to characterize the phase of sample. Thermodynamic calculations based on the CalPhaD method were performed using ThermoCalc software coupled with TCHEA 5.1 HEA database.

The mechanical characterization was performed by means of microhardness measurements using a Clemex CMT (v. 8.0.197) microhardness machine, with a force load of 25 g and a dwell time of 10 s. Nano-indentation was also performed via an iMicro Nanoindenter, where a force load of 50 mN was applied in each consecutive indentation. A homemade linear pin-on-disk wear tester was used for the wear test using a WC pin, with a force load of 981.2 g for 100 cycles (200 passes) with 7 mm of single travel distance. Finally, wear resistance was measured by comparing the depth and width of the wear track using a Keyence VK-X250 laser profilometer.

3. Results and discussion

3.1. Microstructure analysis

An OM image of the cross-section of the AD coating is shown in Fig. 1a, clearly illustrating the coating-substrate interface. Three types of defects are present in the coating, cracks, voids, and oxides, as highlighted in the image. The formation of voids and oxides is an inherent trade-off in the ESD process [18]. Higher pulse energy and power input result in elevated local temperatures and faster solidification rates, which promote the formation of oxides and cracks [19]. Conversely, lower energy input limits material transfer from the electrode, leading to insufficient filling and the formation of voids. Crack formation is closely related to the splat geometry, which typically features a thicker center and thinner edges. The thinner edges cool more rapidly due to their lower material volume, creating a thermal gradient within the splat during solidification. This gradient induces horizontal tensile residual stresses upon cooling and contraction, ultimately leading to vertical crack formation [19]. Therefore, a balanced parameter set of 100 μF, 80 V, 120 Hz was employed to fabricate a high-quality coating with a low defect rate. However, despite this optimization, the formation of cracks, voids, and oxides could not be entirely avoided due to the inherent trade-off in the process.

Table 1
Parameters trials during ESD process of AlCrFeCoNi HEA coating fabrication.

Capacitance [μF]	Voltage [V]	Frequency [Hz]
80–120	80–120	100–170

Fig. 1b shows the etched cross-section of the AD samples, with cellular grains are aligned perpendicularly to the electrode's travel direction. This alignment is attributed to epitaxial growth during the solidification of the liquidus material [20]. A closer examination via SEM, as shown in Fig. 1c, highlights these grains, along with individual splats whose boundaries are delineated by yellow dotted lines. The splat boundaries illustrate different morphology as the boundaries undergo a secondary melting and solidification during the continuous deposition. The cellular grains span multiple splat boundaries due to epitaxial growth, where molten material from the electrode aligns with the orientation of the previously deposited layer [20]. The width of these grains ranges from 1 to 10 μm, with most measuring approximately 3 μm, and their length extending through the entire thickness of the coating. EDX mapping of the area shown in Fig. 1d (presented in Fig. 1e) reveals no evident elemental segregation among the grains or along the grain boundaries (GBs). XRD analysis of the AD coating is shown in Fig. 1f. Peaks at 31.5°, 44.7°, 65.9°, and 82.7°, corresponding to the (100), (110), (200), and (211) planes, respectively, of the BCC phase, with the (200) peak exhibiting the highest intensity.

The Inconel 718 substrate exhibits a microstructure characterized by equiaxed grains. In contrast, the region near the interface presents a distinct morphological transition, as delineated by the dashed lines in Fig. 2a. During the ESD process, both the electrode and substrate materials undergo localized melting, followed by mixing and rapid solidification, resulting in the formation of a metallurgical bond. On the substrate side of the interface, cellular grains with varied orientations are observed, distinguished by the alignment of subgrains, as highlighted by the arrows in Fig. 2b. This microstructural pattern is characteristic of deposited Inconel 718, consistent with previous findings [18,21]. Notably, remnants of the original equiaxed grains remain visible beneath the subgrain structure, as illustrated in Fig. 2c.

Fig. 3a presents the EBSD phase map of the AD HEA coating and the substrate, revealing that the entire coating consists of BCC phase. Due to the small volume of material transferred from the electrode during ESD and the rapid solidification, the cooling process can be treated analogously to quenching. In an equilibrium system, the phase diagram of AlCrFeCoNi HEA indicates a transformation sequence from a single BCC phase, to dual BCC and FCC phase, to single BCC phase as the material cools from the liquidus state to room temperature [22,23]. However, the rapid cooling rate of the ESD process, a non-equilibrium technique-significantly influences phase formation. It has been reported that at a high cooling rate of 10^5–10^6 K/s during ESD [24], only the BCC phase forms in AlCrFeCoNi HEA [25], consistent with the XRD results shown in Fig. 1f.

The inverse pole figure (IPF) map in Fig. 3b shows cellular grains in the AD coating aligned along the building direction (Y direction, IPFY). The strong alignment to the (100) plane is consistent with the XRD patterns presented in Fig. 1f. Fig. 3c presents the geometrically necessary dislocation (GND) map of the AD coating, highlighting a higher

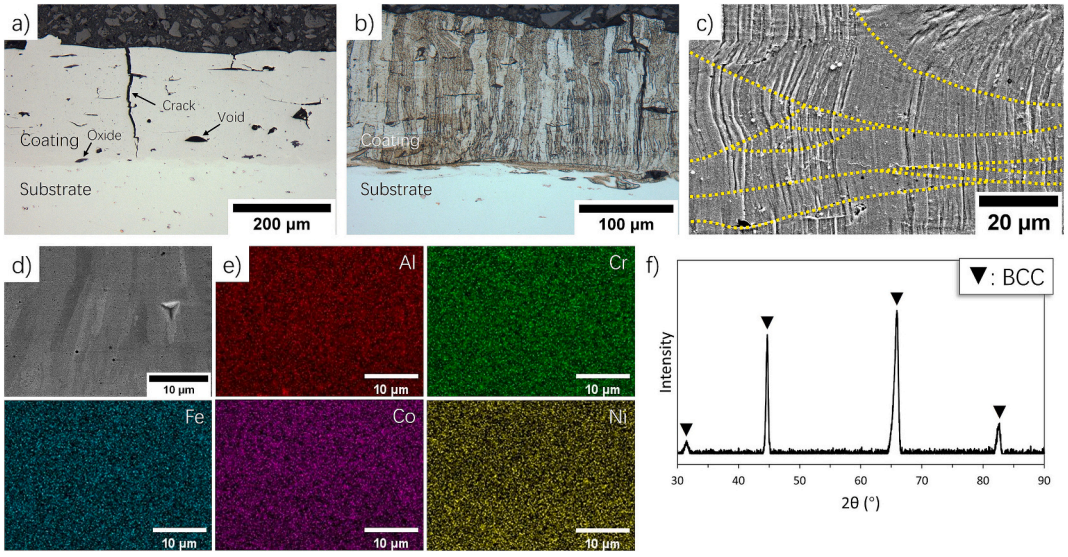

Fig. 1. OM image of the cross-section of a) AD coating highlighting defects characteristic of the process and b) etched cross-section; c) SEM image of etched cross-section; d) BSE image of the AD coating that contains multiple cellular grains with e) EDX mapping; f) XRD spectrum of AD coating and g) magnified range of (200) plane peak; f) XRD spectrum of AD coating.

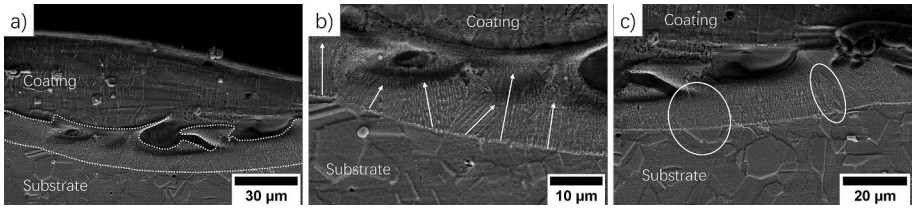

Fig. 2. SEM images of a) morphology of interfacial layer circled with white dot lines; magnified view of interfacial layer that shows the b) orientation of the secondary patterns and c) residual microstructure of the Inconel 718 substrate.

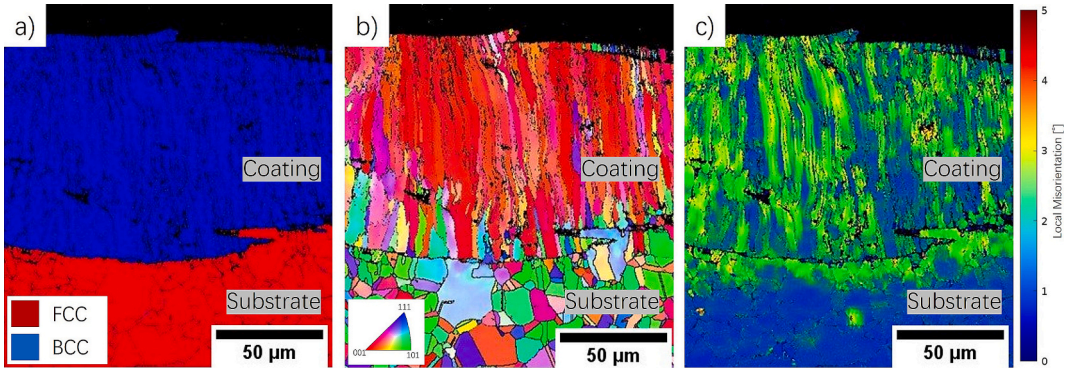

Fig. 3. EBSD analysis of AD coating with a) phase map that shows single BCC phase coating and FCC substrate; b) IPF map where the grain orientation along Y direction; and c) GND map that shows higher density of dislocation in the coating and substrate areas near the interfacial layer.

dislocation density in both the coating and the near-interface region of the substrate, extending to a depth of approximately 20 μm. This increased dislocation density is attributed to the rapid solidification and cooling rate inherent to the ESD process. The depth of the high dislocation density area in the substrate corresponds to the heat-affected zone (HAZ) observed in Fig. 2. Additionally, the IPFY map reveals that the grain orientation of the substrate near the interface remains equiaxed, with only slight misorientation indicated by subtle color variations within the grains. This observation is consistent with the original equiaxed structure shown in Fig. 2c.

Studies have reported that equiatomic AlCrFeCoNi HEA is known as a multi-phase HEA, where phase transformation occurs at elevated temperatures [8,16,17]. The AD AlCrFeCoNi HEA coating, characterized by the BCC phase due to the rapid cooling from liquidus state to room temperature, exhibits high residual stresses and is more suspectable to cracks during the ESD process. Therefore, heat treatment was conducted at 1050 °C for 4 h for phase transformation and stress relieve to improve the coating properties in modulus and wear resistance, where FCC phase with a higher ductility can be formed according to the phase diagram of the HEA [22].

XRD analysis was performed exclusively on the HT coating, as shown in Fig. 4a. The diffraction peaks reveal the presence of at least three phases in the HT coating. The FCC phase is identified by peaks at 2θ values of 43.6°, 50.7°, and 74.7°, corresponding to the (111), (200), and

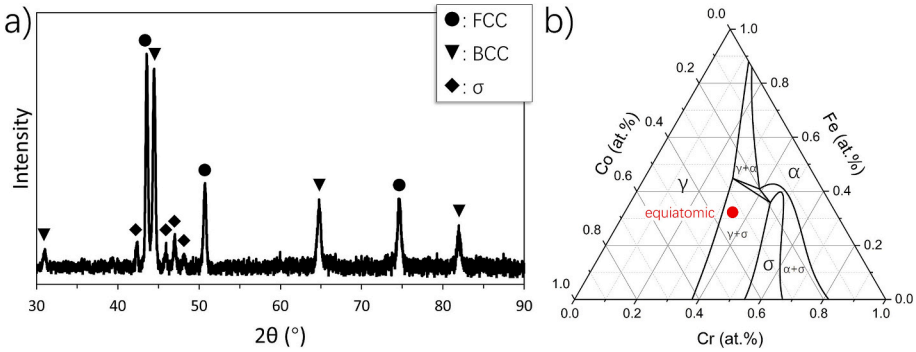

Fig. 4. a) XRD spectrum of the HT coating where FCC, BCC, and σ phases are indicated; b) ternary phase diagram of Cr-Fe-Co system where equiatomic condition is identified in the γ/σ (FCC/σ) mixing region.

(220) planes, respectively. Peaks at 31.1°, 44.5°, 64.7°, and 81.9° are attributed to the (100), (110), (200), and (211) planes of the BCC phase. Additionally, small peaks observed between 40° and 50° suggest the presence of the σ phase [25]. Fig. 4b presents a calculated ternary phase diagram of the Cr–Fe–Co system at 1050 °C, showing that the equiatomic composition lies within the dual-phase region of σ and γ (FCC). The equiatomic point is positioned near the FCC region, indicating that the FCC phase is predominant.

The BSE image of the cross-section of the HT coating is shown in Fig. 5a, revealing multiple cellular grains with dendritic bright regions at the GBs. Elemental analysis was conducted at three locations labeled in Fig. 5a: location 1 corresponds to the FCC phase, location 2 to the σ phase, and location 3 to the dark matrix. The atomic fractions of the elements at these locations are detailed in Table 2. The σ phase is characterized by a high Cr content and a depletion of Al and Ni, with atomic ratios of Cr, Fe, and Co approximately 2.2:1.2:1. Similarly, the FCC phase is also depleted of Al and Ni, with Cr, Fe, and Co in a molar ratio of approximately 1.1:1.2:1, consistent with the phase diagram presented in Fig. 4b. EBSD analysis was performed in the circled region, with the IPFY map and phase map shown in Fig. 5b and c, respectively. These maps indicate that the FCC phase primarily forms dendritically along the GBs, with a width of approximately 1 μm. The GBs also contain the σ phase, and both FCC and σ phases are observed within the grains as fragments smaller than 1 μm embedded in the matrix. The EDX map in Fig. 5d further confirms the high Cr content in the σ phase and the low Al and Ni content in the FCC phase. Additionally, regions enriched in Al and Ni, with an atomic ratio of approximately 1:1, are identified as the BCC AlNi phase [26,27], with Cr, Fe, and Co dissolved in solid solution [28].

Table 2
Chemical composition in the locations labeled in Fig. 5a in at.%.

Locations	Al	Cr	Fe	Co	Ni	Phase
1	9.1	24.3	26.5	22.6	17.5	FCC
2	7.2	41.2	22.8	19.7	9.1	σ
3	31.0	11.0	12.5	17.6	27.9	BCC

The sluggish diffusion effect of HEAs results in a slower diffusion rate for less-active elements. Consequently, the diffusion of Ni from low-energy sites (within the grains) to high-energy sites (GBs) is impeded, allowing only one-way diffusion of Ni from the GBs into the grains. This promotes the diffusion of more active elements, such as Cr, from the grain interior toward the GBs. This phenomenon accounts for the formation of Cr-rich σ and FCC phases at the GBs. As a result, Ni becomes enriched within the grains, hindering Cr accumulation and facilitates the stabilization of the active element aluminum (Al) by forming the AlNi phase. This phase is thermodynamically favored due to its low mixing enthalpy of −22 kJ/mol [29]. Additionally, the grain width increases to approximately 6 μm during the heat treatment.

Fig. 6a presents the BSE image of the overall cross-section from the HT substrate to coating. Fig. 6b and c provide magnified views of the substrate–interfacial layer (IL) interface and IL-coating interface, respectively. These images illustrate the phase transition from the substrate to the IL and the precipitation mechanism of dendritic FCC/σ phases originating from the IL.

The EBSD phase map in Fig. 6d reveals that the phase of the substrate

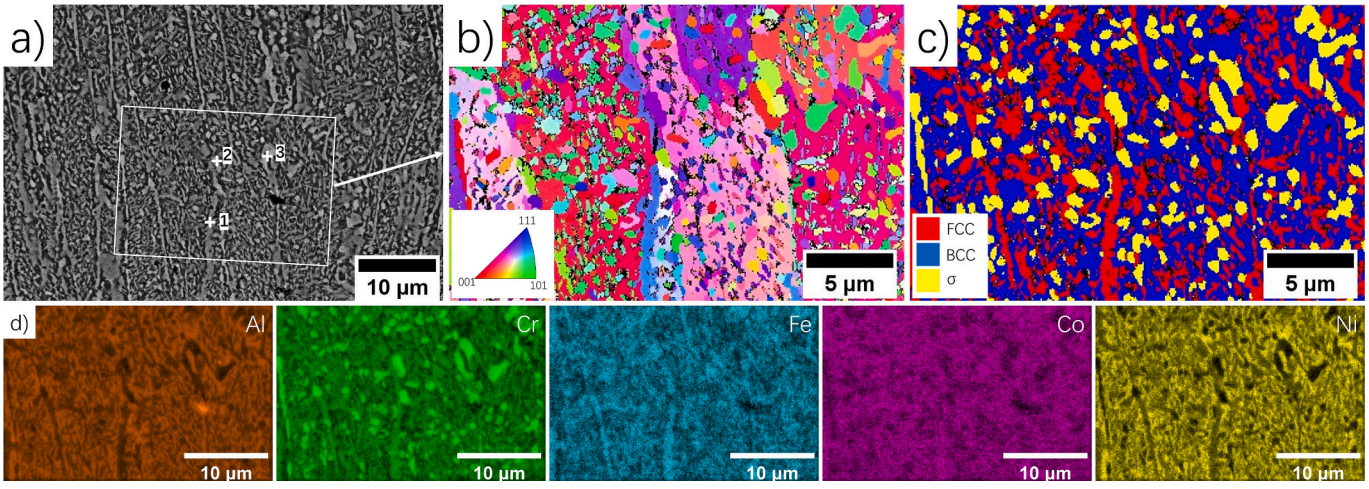

Fig. 5. a) BSE image of the HT coating where phase transformation shown in different contrast; b) IPF map along Y direction; c) phase map with FCC, BCC and σ phases indicated; and d) elemental map of Al, Cr, Fe, Co, and Ni the circled area in a).

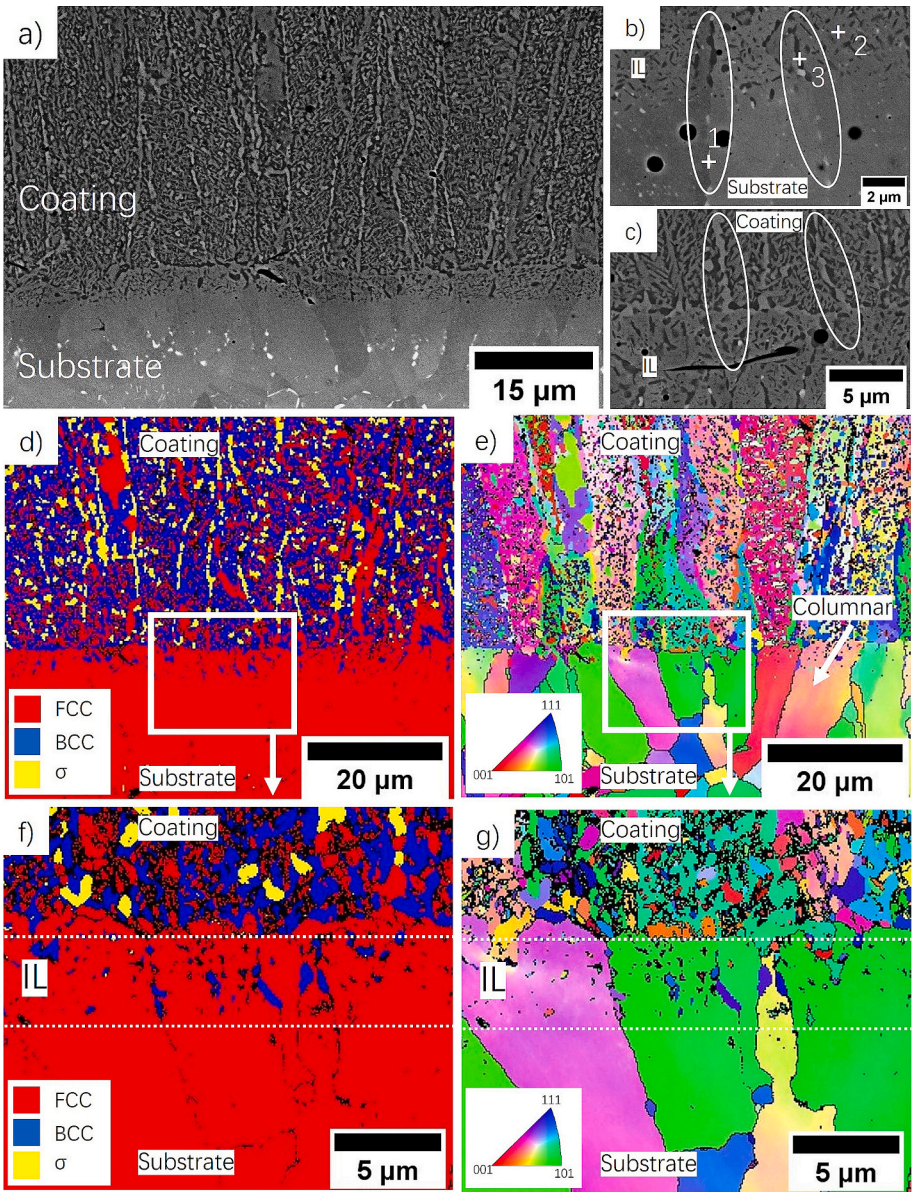

Fig. 6. BSE image of the a) HT coating and substrate and magnified area of HT coating at the interface between b) substrate/interfacial layer and c) interfacial layer/coating; EBSD d) phase and e) IPFY map of HT coating and substrate; EBSD f) phase and g) IPFY map on magnified area circled in d) and e).

near the interface remains unchanged after heat treatment. In the AD coating, as shown in Figs. 2 and 3, the substrate near the IL exhibits original equiaxed grains beneath the subgrain structure. However, the IPFY map of the HT coating in Fig. 6e demonstrates that these equiaxed grains have fully reoriented into cellular grains. This observation suggests that heat treatment has a more significant effect on equiaxed grains compared to cellular grains in the Inconel 718 system [30].

Three specific locations are marked in Fig. 6b for detailed analysis: location 1 corresponds to a high-brightness region within the substrate, while locations 2 and 3 denote bright and dark regions within the IL, respectively. EDS analysis was conducted on these locations, and the atomic compositions are summarized in Table 3. Location 1 reveals the presence of the Laves phase in Inconel 718, characterized by high brightness in the BSE image and enrichment in Nb and Mo. These phases are primarily located at the cellular GBs within the substrate. The cellular grains themselves are identified as FCC phase, as shown in the EBSD phase map in Fig. 6f. These grains extend into the IL, where most regions consist of FCC phase due to epitaxial growth, consistent with the chemical composition observed at location 2. However, a phase transition is observed at the grain boundaries of the cellular grains from the substrate to the IL, as indicated by the circled area in Fig. 6b. At these GBs (location 3), the IL exhibits a BCC phase, reflecting the segregation

Table 3
Chemical composition of the locations labeled in Fig. 6b and c in at.%.

Locations	Al	Ti	Cr	Fe	Co	Ni	Nb	Mo	Phase
1	–	0.8	22.1	19.7	–	36.3	13.4	7.7	Laves
2	9.6	–	22.6	22.1	12.2	33.5	–	–	FCC
3	22.3	–	14.9	15.5	11.1	36.2	–	–	BCC

of dissimilar phases to the GBs as a result of epitaxial growth. Furthermore, the BCC phase appears more randomly distributed within the IL near the coating side, initiating precipitation growth in the HT coating, as illustrated in Fig. 6c.

Given that the majority of the IL consists of the FCC phase, heat treatment promotes the dendritic growth of phases with similar chemical compositions into the coating. During this process, elements in the AD system diffuse in opposite directions: Cr diffuses in one direction, while Al and Ni diffuse in the opposite direction. This diffusion pattern results in the formation of dendritic σ or FCC phases at the GBs, as highlighted in the circled areas in Fig. 6c, along with a BCC matrix within the grains. Additionally, fragmental FCC precipitates, smaller than 1 μm, form within these grains.

3.2. Mechanical properties

Nano-indentation was conducted on the coating, interface, and substrate areas of both the AD and HT samples, as illustrated in Fig. 7a and d, respectively. The load-displacement curves for the AD sample are presented in Fig. 7b, revealing maximum indenter penetrations of 722 nm, 661 nm, and 568 nm for the substrate, interface, and coating, respectively. These results indicate that the AD HEA coating exhibits the least plastic deformation among the three regions.

The formation of nano-sized precipitates and the presence of wider cellular grains after heat treatment introduce competing effects on hardness. While nano-sized precipitates tend to increase hardness, wider cellular grains typically reduce it. In the AD coating, the unloading curve exhibits the lowest elastic region, indicated by the lowest slope in the unloading region. Fig. 7c illustrates the hardness and modulus versus depth for the AD sample, respectively, revealing that the coating exhibits the highest hardness (7.07 GPa) and the lowest modulus (164.50 GPa) among the three regions. In the HT sample (Fig. 7e), the coating also shows the lowest indenter penetration (548 nm), indicating greater hardness than the AD coating, and similarly displays the least elastic region. The depth-dependent hardness and modulus profile further demonstrates that the HT coating exhibits increased hardness (7.42 GPa) and modulus (206.46 GPa). The increase in hardness is attributed to phase transformations induced by heat treatment, while the increase in modulus is attributed to the release of residual stresses accumulated during the ESD process and the formation of the higher-ductility FCC phase during heat treatment.

Fig. 8a depicts the microhardness profiles of both the AD and HT coatings along the substrate. Negative distances indicate depths from the indenter in the coating side toward the interface, while positive distances represent penetration into the substrate, with the interface between the coating and IL marked as 0 distance. The AD coating exhibits a microhardness of approximately 550 Hv, whereas the HT coating shows a reduced microhardness of around 440 Hv. This reduction is attributed to the growth of cellular grains and the formation of the ductile FCC phase, as identified in the EBSD analyses (Figs. 3 and 4). The gradual decrease in microhardness from 25 μm to the interface in the coating results from substrate element dilution into the coating. At 10 μm from the substrate interface, a critical HAZ is evident, characterized by cellular grains with higher microhardness compared to the bulk Inconel 718. Additionally, a subcritical HAZ extending approximately 40 μm is observed due to heat input during the ESD process. EBSD analysis indicate no significant grain growth occurs during heat treatment. Comparatively, the microhardness of the HT bulk substrate is slightly higher than that of the AD substrate. This increase is attributed to the formation of σ phase precipitates, as shown in Fig. 8b (indicated by arrows), primarily located at grain boundaries due to Nb migration during heat treatment, resulting in σ-Ni_3Nb phase formation [31].

The comparison of hardness between the AD and HT coatings, measured through both nano-indentation and microhardness, reveals contrasting trends. Microhardness measurements show that the AD coating is 110 Hv harder than the HT coating. Conversely, nano-indentation results indicate that the HT coating exhibits a higher hardness by 0.35 GPa compared to the AD coating. This discrepancy arises

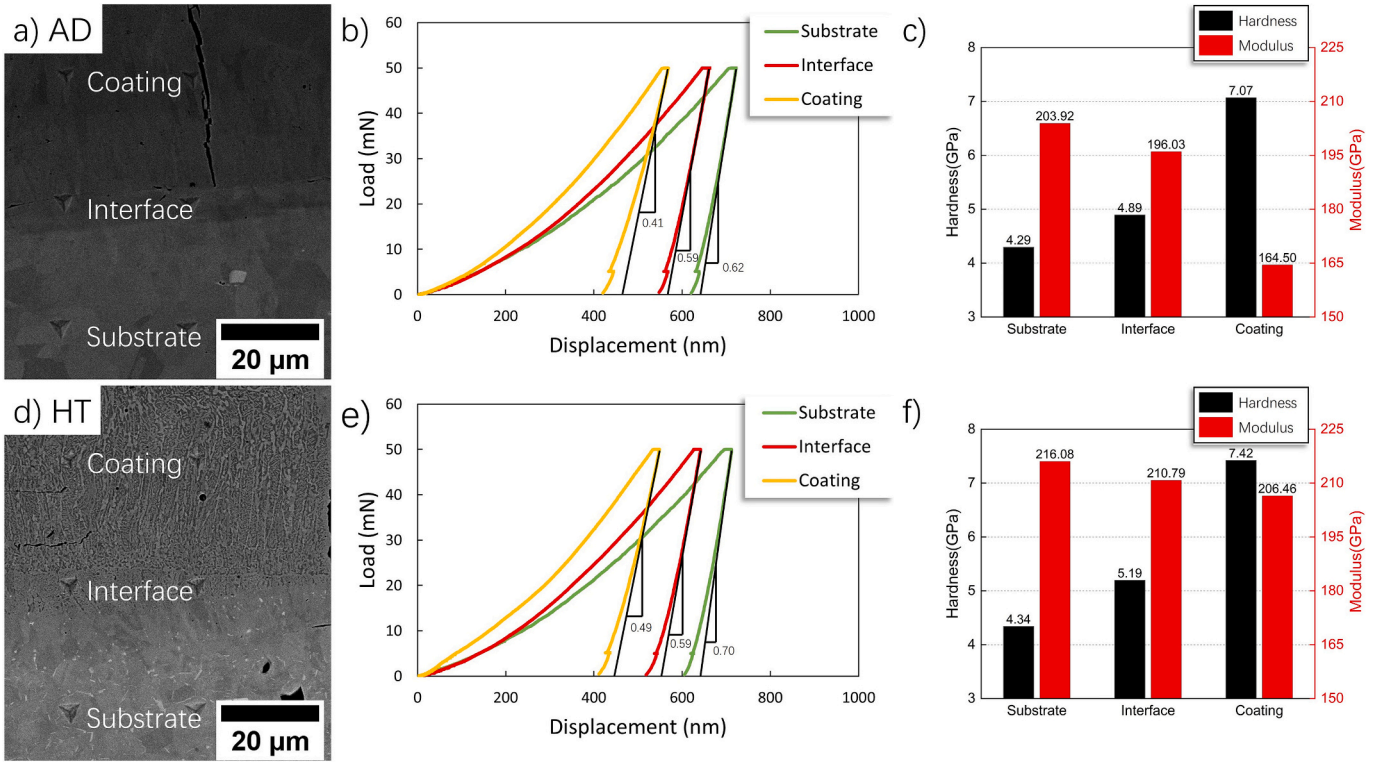

Fig. 7. a) and b) Indenter of nano-indentation of AD and HT specimen at coating, interface, and substrate; b) and e) force load versus displacement; c) and f) relationships of hardness and elastic modulus of AD and HT coatings, respectively.

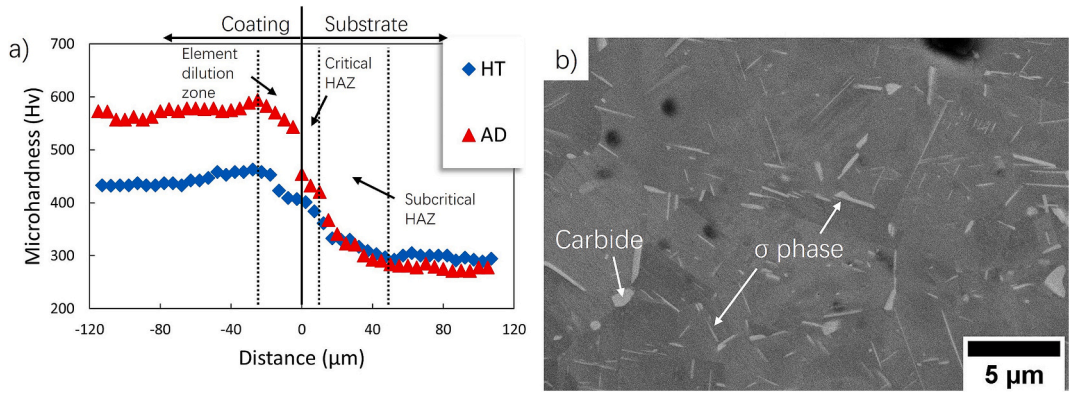

Fig. 8. a) microhardness profile of AD and HT coating from coating to substrate; b) heat treated substrate with carbide and σ phase precipitates formation indicated which leads to slight increase in hardness.

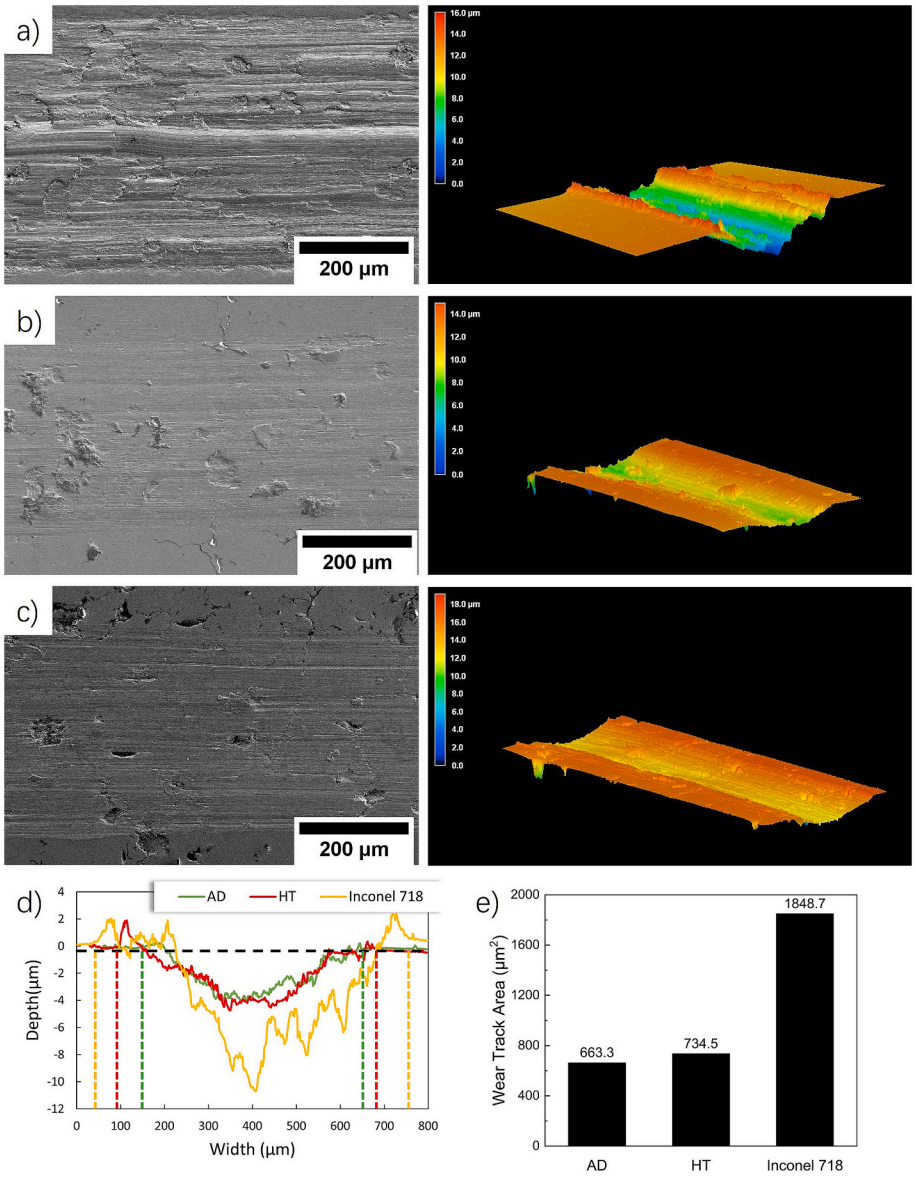

Fig. 9. SEM images of wear test of a) Inconel 718; b) AD coating; c) HT coating with 3D height schema of the wear track; d) height profile of the cross-section of the wear track at random location; e) diagram of areas of the cross-section of the wear track.

from differences in the measurement scales and sensitivities of the two techniques. Microhardness testing involves indenters large enough to span regions wider than the columnar grain width, resulting in plastic deformation across multiple GBs. As a result, the AD coating demonstrates higher microhardness due to its finer grain structure, while the HT coating, having undergone transformation into the more ductile FCC phase along the GBs and grain coarsening, exhibits reduced microhardness. In contrast, nano-indentation involves much smaller and shallower indenters, enabling localized measurements within individual microstructural features. In the AD coating, nano-indentation primarily probes within individual grains, capturing their intrinsic hardness. In the HT coating, however, the indenter often spans multiple phases and phase boundaries, including hard σ precipitates and phase interfaces, which contribute to the higher measured hardness.

Regarding the substrate, both nano-indentation and microhardness measurements indicate higher hardness, primarily due to the formation of secondary phases. This aligns with observations in Fig. 8b, where the formation of σ-Ni_3Nb phase precipitates at grain boundaries contributes to increased substrate hardness.

The wear test was conducted on the Inconel 718 substrate, as well as the AD and HT coatings. SEM images depicting the wear tracks are presented in Fig. 9a-c, accompanied by 3D models. Fig. 9d displays the cross-sectional height profiles of the wear tracks, revealing that the AD coating exhibits the shallowest depth and narrowest width, indicative of superior wear resistance. Fig. 9e shows the wear track area cross-sections, facilitating the calculation of the specific wear rate coefficient, k_w,

$$k_w = \frac{V}{F \times s}$$

Where V denotes the volume of material removed during testing, F represents the applied force load, and s indicates the length of the wear track [32]. By maintaining consistent variables-force load, wear track length, and total test distance, the wear rate difference is reflected by the proportional cross-sectional area of the wear track. The areas are detailed in Fig. 9e, with Inconel 718 exhibiting the highest wear area at 1848.7 μm^2, while the AD and HT coatings display wear areas of 663.3 μm^2 and 734.5 μm^2, respectively. The wear rate demonstrates a 64.12% reduction from the Inconel 718 substrate to the AD AlCrFeCoNi coating, with a subsequent 10.73% increase after heat treatment. The ESD process generates substantial tensile residual stresses in the coating due to rapid solidification of the molten material. Studies have shown that these residual stresses detrimentally affect wear resistance [33]. Although heat treatment effectively releases these residual stresses [34], the HT coating exhibits lower wear resistance.

Although the heat treatment resulted in increased nanohardness, wear resistance was slightly better in the AD coating. This suggests that the localized hardening achieved through heat treatment was insufficient to offset the reduction in microhardness and modulus, possibly due to an incomplete phase transformation, grain coarsening, or harmful σ phase formation. To improve wear performance, a more uniform and effective distribution of hard phases needs to be produced, for instance, σ phase can transform to BCC phase for higher wear resistance at elevated temperatures.

4. Conclusion

The homogeneous BCC AD AlCrFeCoNi HEA coating was fabricated using electrospark deposition. The AD coating exhibited cellular grains due to epitaxial growth, with no elemental or phase segregation. Following heat treatment, σ and FCC precipitates formed dendritically at the cellular grain boundaries and then within the cellular grains as fragments within the BCC matrix. The HT coating also displayed cellular grains with a larger grain width. Consequently, the HT coating demonstrated higher hardness in nano-indentation tests but lower microhardness. Additionally, the specific wear rates of the AD and HT coatings were 64.12% and 60.27% lower compared to Inconel 718 substrate, respectively, indicating that the AD coating possessed the highest wear resistance. The results of this study suggest that the AlCrFeCoNi coating fabricated by ESD has significant potential for direct application in wear-resistant contexts, eliminating the need for post-processing.

CRediT authorship contribution statement

Jihui Yan: Writing – original draft, Visualization, Methodology, Investigation, Data curation, Conceptualization. **Joao G. Lopes:** Writing – review & editing, Visualization, Data curation. **Kevin Chan:** Writing – review & editing. **Nigel Scotchmer:** Writing – review & editing. **Joao P. Oliveira:** Writing – review & editing, Supervision. **Y. Norman Zhou:** Writing – review & editing, Supervision, Project administration, Funding acquisition. **Peng Peng:** Writing – review & editing, Supervision, Project administration, Funding acquisition.

Declaration of competing interest

The authors declare that they have no known competing financial interests or personal relationships that could have appeared to influence the work reported in this paper.

Acknowledgements

This work was supported by the Natural Sciences and Engineering Research Council of Canada (NSERC) Alliance grant. JPO acknowledges the funding by national funds from FCT - Fundação para a Ciência e a Tecnologia, I.P., in the scope of the projects LA/P/0037/2020, UIDP/50025/2020 and UIDB/50025/2020 of the Associate Laboratory Institute of Nanostructures, Nanomodelling and Nanofabrication – i3N. JGL acknowledges Fundação para a Ciência e a Tecnologia (FCT - MCTES) for its financial support via the project UID/00667/2020 (UNIDEMI) and for funding the Ph.D. grant 2020.07350.BD.

Data availability

The datasets generated during and/or analyzed during the current study are not publicly available as the data also forms part of an ongoing study but are available from the corresponding author on reasonable request.

References

[1] J.-W. Yeh, S.-K. Chen, S.-J. Lin, J.-Y. Gan, T.-S. Chin, T.-T. Shun, C.-H. Tsau, S.-Y. Chang, Nanostructured high-entropy alloys with multiple principal elements: novel alloy design concepts and outcomes, Adv. Eng. Mater. 6 (2004) 299–303, https://doi.org/10.1002/adem.200300567.

[2] B. Gludovatz, A. Hohenwarter, D. Catoor, E.H. Chang, E.P. George, R.O. Ritchie, A fracture-resistant high-entropy alloy for cryogenic applications, Science 345 (2014) 1153–1158, https://doi.org/10.1126/science.1254581.

[3] O.N. Senkov, S.L. Semiatin, Microstructure and properties of a refractory high-entropy alloy after cold working, J. Alloys Compd. 649 (2015) 1110–1123, https://doi.org/10.1016/j.jallcom.2015.07.209.

[4] Y.D. Wu, Y.H. Cai, T. Wang, J.J. Si, J. Zhu, Y.D. Wang, X.D. Hui, A refractory Hf25Nb25Ti25Zr25 high-entropy alloy with excellent structural stability and tensile properties, Mater. Lett. 130 (2014) 277–280, https://doi.org/10.1016/j.matlet.2014.05.134.

[5] F. Granberg, K. Nordlund, M.W. Ullah, K. Jin, C. Lu, H. Bei, L.M. Wang, F. Djurabekova, W.J. Weber, Y. Zhang, Mechanism of radiation damage reduction in equiatomic multicomponent single phase alloys, Phys. Rev. Lett. 116 (2016) 135504, https://doi.org/10.1103/PhysRevLett.116.135504.

[6] P. Edalati, R. Floriano, A. Mohammadi, Y. Li, G. Zepon, H.-W. Li, K. Edalati, Reversible room temperature hydrogen storage in high-entropy alloy TiZrCrMnFeNi, Scr. Mater. 178 (2020) 387–390, https://doi.org/10.1016/j.scriptamat.2019.12.009.

[7] Y. Xin, S. Li, Y. Qian, W. Zhu, H. Yuan, P. Jiang, R. Guo, L. Wang, High-entropy alloys as a platform for catalysis: progress, challenges, and opportunities, ACS Catal. 10 (2020) 11280–11306, https://doi.org/10.1021/acscatal.0c03617.

[8] Y.P. Wang, B.S. Li, M.X. Ren, C. Yang, H.Z. Fu, Microstructure and compressive properties of AlCrFeCoNi high entropy alloy, Mater. Sci. Eng. A 491 (2008) 154–158, https://doi.org/10.1016/j.msea.2008.01.064.
[9] Y.-F. Kao, T.-J. Chen, S.-K. Chen, J.-W. Yeh, Microstructure and mechanical property of as-cast, −homogenized, and -deformed AlxCoCrFeNi (0≤x≤2) high-entropy alloys, J. Alloys Compd. 488 (2009) 57–64, https://doi.org/10.1016/j.jallcom.2009.08.090.
[10] M. Löbel, T. Lindner, T. Mehner, L.-M. Rymer, S. Björklund, S. Joshi, T. Lampke, Microstructure and corrosion properties of AlCrFeCoNi high-entropy alloy coatings prepared by HVAF and HVOF, J. Therm. Spray Technol. 31 (2022) 247–255, https://doi.org/10.1007/s11666-021-01255-2.
[11] M. Löbel, T. Lindner, S. Clauß, R. Pippig, D. Dietrich, T. Lampke, Microstructure and wear behavior of the high-velocity-oxygen-fuel sprayed and spark plasma sintered high-entropy alloy AlCrFeCoNi, Adv. Eng. Mater. 23 (2021) 2001253, https://doi.org/10.1002/adem.202001253.
[12] D. Chen, Y. Guan, G. Jin, X. Cui, E. Liu, L. Feng, X. Li, In-situ synthesis of a FeCoCrNiCu/FeCoCrNiAl composite high entropy alloy coating by laser cladding, Surf. Coat. Technol. 461 (2023) 129447, https://doi.org/10.1016/j.surfcoat.2023.129447.
[13] N. Noble, N. Radhika, M. Sathishkumar, B. Saleh, Characterisation and property evaluation of high entropy alloy coating on 316L steel via thermal spray synthesis, Tribol. Int. 185 (2023) 108525, https://doi.org/10.1016/j.triboint.2023.108525.
[14] A. Anupam, S. Kumar, N.M. Chavan, B.S. Murty, R.S. Kottada, First report on cold-sprayed AlCoCrFeNi high-entropy alloy and its isothermal oxidation, J. Mater. Res. 34 (2019) 796–806, https://doi.org/10.1557/jmr.2019.38.
[15] C. Barile, C. Casavola, G. Pappalettera, G. Renna, Advancements in electrospark deposition (ESD) technique: a short review, Coatings 12 (2022) 1536, https://doi.org/10.3390/coatings12101536.
[16] A. Manzoni, H. Daoud, R. Völkl, U. Glatzel, N. Wanderka, Phase separation in equiatomic AlCoCrFeNi high-entropy alloy, Ultramicroscopy 132 (2013) 212–215, https://doi.org/10.1016/j.ultramic.2012.12.015.
[17] M.E. Bloomfield, K.A. Christofidou, P.M. Mignanelli, A.-P.M. Reponen, H.J. Stone, N.G. Jones, Phase stability of the AlxCrFeCoNi alloy system, J. Alloys Compd. 926 (2022) 166734, https://doi.org/10.1016/j.jallcom.2022.166734.
[18] J. Yan, P.D. Enrique, K. Chan, N. Scotchmer, P. Peng, N.Y. Zhou, Repair of additive manufactured thin-wall geometry using electrospark deposition, J. Remanuf. 13 (2023) 333–353, https://doi.org/10.1007/s13243-023-00133-0.
[19] L.M. Felix, C.C.F. Kwan, N.Y. Zhou, The effect of pulse energy on the defects and microstructure of electro-spark-deposited Inconel 718, Metall. Mater. Trans. A 50 (2019) 4223–4231, https://doi.org/10.1007/s11661-019-05332-8.
[20] S. Kou, Welding Metallurgy, 2nd ed, Wiley-Interscience, Hoboken, N.J, 2003.
[21] P.D. Enrique, Z. Jiao, N.Y. Zhou, Effect of direct aging on heat-affected zone and tensile properties of electrospark-deposited alloy 718, Metall. Mater. Trans. A 50 (2019) 285–294, https://doi.org/10.1007/s11661-018-4997-1.
[22] S. Yang, J. Lu, F. Xing, L. Zhang, Y. Zhong, Revisit the VEC rule in high entropy alloys (HEAs) with high-throughput CALPHAD approach and its applications for material design-a case study with Al–Co–Cr–Fe–Ni system, Acta Mater. 192 (2020) 11–19, https://doi.org/10.1016/j.actamat.2020.03.039.
[23] X. Zhang, L. Liu, K. Yao, K. Duan, F. Wu, R. Zhao, Y. Zhang, J. Shang, M. Chen, The phase composition characteristics of AlCoCrFeNi high entropy alloy heat-treated by simple normalizing treatment and its effects on mechanical properties, J. Alloys Compd. 926 (2022) 166896, https://doi.org/10.1016/j.jallcom.2022.166896.
[24] Y. Xie, M. Wang, Isothermal oxidation behavior of electrospark deposited MCrAlX-type coatings on a Ni-based superalloy, J. Alloys Compd. 480 (2009) 454–461, https://doi.org/10.1016/j.jallcom.2009.01.100.
[25] M.-H. Tsai, K.-Y. Tsai, C.-W. Tsai, C. Lee, C.-C. Juan, J.-W. Yeh, Criterion for sigma phase formation in Cr- and V-containing high-entropy alloys, Mater. Res. Lett. 1 (2013) 207–212, https://doi.org/10.1080/21663831.2013.831382.
[26] K. Bochenek, M. Basista, Advances in processing of NiAl intermetallic alloys and composites for high temperature aerospace applications, Prog. Aerosp. Sci. 79 (2015) 136–146, https://doi.org/10.1016/j.paerosci.2015.09.003.
[27] Q. Song, C. Li, Z. Deng, L. Zhang, L. Liu, Experimental investigation and thermodynamic assessment of the ternary Al–Ni–Er system, Processes 11 (2023) 1061, https://doi.org/10.3390/pr11041061.
[28] C. Li, J.C. Li, M. Zhao, Q. Jiang, Effect of aluminum contents on microstructure and properties of AlxCoCrFeNi alloys, J. Alloys Compd. 504 (2010) S515–S518, https://doi.org/10.1016/j.jallcom.2010.03.111.
[29] A. Takeuchi, A. Inoue, Classification of bulk metallic glasses by atomic size difference, heat of mixing and period of constituent elements and its application to characterization of the main alloying element, Mater. Trans. 46 (2005) 2817–2829, https://doi.org/10.2320/matertrans.46.2817.
[30] E. Anisimov, A.K. Khan, O.A. Ojo, Analysis of microstructure in electro-spark deposited IN718 superalloy, Mater. Charact. 119 (2016) 233–240, https://doi.org/10.1016/j.matchar.2016.07.025.
[31] X. Xie, G. Wang, J. Dong, C. Xu, W.-D. Cao, R. Kennedy, Structure Stability Study on a Newly Developed Nickel-Base Superalloy - Allvac 718Plus, in: Superalloys 718 625 706 Var. Deriv. 2005, TMS, 2005, pp. 179–191, https://doi.org/10.7449/2005/Superalloys_2005_179_191.
[32] D. Shekhawat, P. Agarwal, T. Singh, A. Singh, A. Patnaik, Effect of control factors on wear rate of the ceramic particulate filled metal alloy composites: a comparative analysis, Arab. J. Sci. Eng. 48 (2023) 11819–11840, https://doi.org/10.1007/s13369-022-07576-w.
[33] W. Luo, U. Selvadurai, W. Tillmann, Effect of residual stress on the wear resistance of thermal spray coatings, J. Therm. Spray Technol. 25 (2016) 321–330, https://doi.org/10.1007/s11666-015-0309-0.
[34] M. Landwehr, F. Oehler, H. Behnken, H. Holling, R. Sambathkumar, P. Ganser, T. Bergs, Influence of heat treatment on the residual stress-related machining distortion of Ti-6Al-4V alloy monolithic parts, Procedia CIRP 104 (2021) 1328–1333, https://doi.org/10.1016/j.procir.2021.11.223.